# Experimental and computational analysis of the transition state for ribonuclease A-catalyzed RNA 2′-*O*-transphosphorylation

Hong Gu[a], Shuming Zhang[a], Kin-Yiu Wong[b,c], Brian K. Radak[b,d], Thakshila Dissanayake[b], Daniel L. Kellerman[a], Qing Dai[e], Masaru Miyagi[f], Vernon E. Anderson[a], Darrin M. York[b,1], Joseph A. Piccirilli[e,g,1], and Michael E. Harris[a,1]

[a]Department of Biochemistry and [f]Center for Proteomics and Bioinformatics, Case Western Reserve University School of Medicine, Cleveland, OH 44106; [b]Center for Integrative Proteomics Research, Biology at the Interface with the Mathematical and Physical Sciences (BioMaPS) Institute for Quantitative Biology and Department of Chemistry and Chemical Biology, Rutgers, The State University of New Jersey, Piscataway, NJ 08854; Departments of [e]Chemistry and [g]Biochemistry and Molecular Biology, University of Chicago, Chicago, IL 60637; [c]Department of Physics, High Performance Cluster Computing Centre, Institute of Computational and Theoretical Studies, Hong Kong Baptist University, Kowloon Tong 852, Hong Kong; and [d]Department of Chemistry, University of Minnesota, Minneapolis, MN 55455

Edited by Philip C. Bevilacqua, The Pennsylvania State University, University Park, PA, and accepted by the Editorial Board June 17, 2013 (received for review September 5, 2012)

**Enzymes function by stabilizing reaction transition states; therefore, comparison of the transition states of enzymatic and nonenzymatic model reactions can provide insight into biological catalysis. Catalysis of RNA 2′-*O*-transphosphorylation by ribonuclease A is proposed to involve electrostatic stabilization and acid/base catalysis, although the structure of the rate-limiting transition state is uncertain. Here, we describe coordinated kinetic isotope effect (KIE) analyses, molecular dynamics simulations, and quantum mechanical calculations to model the transition state and mechanism of RNase A. Comparison of the $^{18}$O KIEs on the 2′O nucleophile, 5′O leaving group, and nonbridging phosphoryl oxygens for RNase A to values observed for hydronium- or hydroxide-catalyzed reactions indicate a late anionic transition state. Molecular dynamics simulations using an anionic phosphorane transition state mimic suggest that H-bonding by protonated His12 and Lys41 stabilizes the transition state by neutralizing the negative charge on the nonbridging phosphoryl oxygens. Quantum mechanical calculations consistent with the experimental KIEs indicate that expulsion of the 5′O remains an integral feature of the rate-limiting step both on and off the enzyme. Electrostatic interactions with positively charged amino acid site chains (His12/Lys41), together with proton transfer from His119, render departure of the 5′O less advanced compared with the solution reaction and stabilize charge buildup in the transition state. The ability to obtain a chemically detailed description of 2′-*O*-transphosphorylation transition states provides an opportunity to advance our understanding of biological catalysis significantly by determining how the catalytic modes and active site environments of phosphoryl transferases influence transition state structure.**

Enzymes achieve powerful rate enhancements by providing multiple catalytic modes to stabilize reaction transition states, including electrostatic interactions and proton transfer (1). For RNA 2′-*O*-transphosphorylation reactions, interactions with acid, base, or metal ion catalysts in solution can influence transition state structure (2). Understanding biological catalysis therefore requires knowledge of chemical mechanisms, transition state structure, and transition state interactions for both enzymatic and nonenzymatic RNA cleavage reactions. Comparisons of enzymatic and nonenzymatic catalysis can provide information on which catalytic modes are used by enzymes and whether unique features of the active site environment may alter the transition state charge distribution (3).

RNA undergoes two competing transesterification reactions in solution: isomerization to a 2′,5′-phosphodiester and 2′-*O*-transphosphorylation to yield a cyclic 2′,3′-phosphodiester with concomitant release of the 5′O-nucleoside (4, 5). Reactions catalyzed by acid and by buffers yield both isomerization and cleavage products and proceed via a pentacoordinated phosphorane intermediate formed by an attack of the 2′OH at the adjacent phosphorus. The phosphorane intermediate may be neutral ($I_{neutral}$) (Fig. S1*A*) or monoanionic ($I_{monoanion}$) (Fig. S1*B*). It is not known whether 2′OH deprotonation occurs in a preequilibrium step or if its proton is transferred to water or one of the nonbridging phosphoryl oxygens (NPOs) during nucleophilic attack. Hydroxide catalysis proceeds by equilibrium deprotonation of the 2′OH, followed by nucleophilic attack (Fig. S1*C*), and only cleavage products are formed (5, 6). Linear free energy relationships (LFERs), stereochemical outcomes, kinetic isotope effects (KIEs), and computational simulations are consistent with either an overall concerted mechanism or transient formation of a dianionic phosphorane intermediate (>pH 9) (4, 5). This complex mechanistic landscape raises the question of which pathway(s) are favored by the active sites of ribonucleases.

RNase A catalyzes RNA 2′-*O*-transphosphorylation, and investigation of its structure and function have provided foundational insights into the function of enzyme active site residues in acid/base catalytic modes (7). Although the mechanism is usually depicted as concerted, computational studies suggest the potential for a stepwise mechanism via an anionic phosphorane intermediate (8) (Fig. 1*A*, top pathway). Molecular dynamics (MD) simulations indicate that the RNase A active site provides electrostatic stabilization of the dianionic phosphorane while positioning His119 to act as a general acid (9). His12 and Lys41 are proposed to interact with the 2′OH and/or one of the NPOs, possibly stabilizing the transition state for nucleophilic attack (TS1) or anionic intermediates via H-bonding or proton transfer to form $I_{neutral}$ or $I_{monoanion}$. However, lack of a strong thio effect renders the latter mode unlikely (10). Several lines of evidence implicate His119 as a general acid to facilitate departure of the 5′O in a stepwise or concerted mechanism [via a product-like transition state (TS2) or a concerted transition state ($TS_c$)]. Mutation of His119 has a large deleterious effect on catalysis of RNA cleavage but only a small effect on the reaction of a uridine-3′-*p*-nitrophenol phosphate model substrate, consistent with

Author contributions: H.G., V.E.A., D.M.Y., J.A.P., and M.E.H. designed research; H.G., S.Z., K.-Y.W., B.K.R., T.D., D.L.K., V.E.A., and M.E.H. performed research; Q.D. and M.M. contributed new reagents/analytic tools; H.G., S.Z., K.-Y.W., B.K.R., T.D., D.L.K., V.E.A., D.M.Y., J.A.P., and M.E.H. analyzed data; and H.G., S.Z., D.M.Y., J.A.P., and M.E.H. wrote the paper.

The authors declare no conflict of interest.

This article is a PNAS Direct Submission. P.C.B. is a guest editor invited by the Editorial Board.

[1]To whom correspondence may be addressed. E-mail: york@biomaps.rutgers.edu, jpicciri@uchicago.edu, or meh2@case.edu.

This article contains supporting information online at www.pnas.org/lookup/suppl/doi:10.1073/pnas.1215086110/-/DCSupplemental.

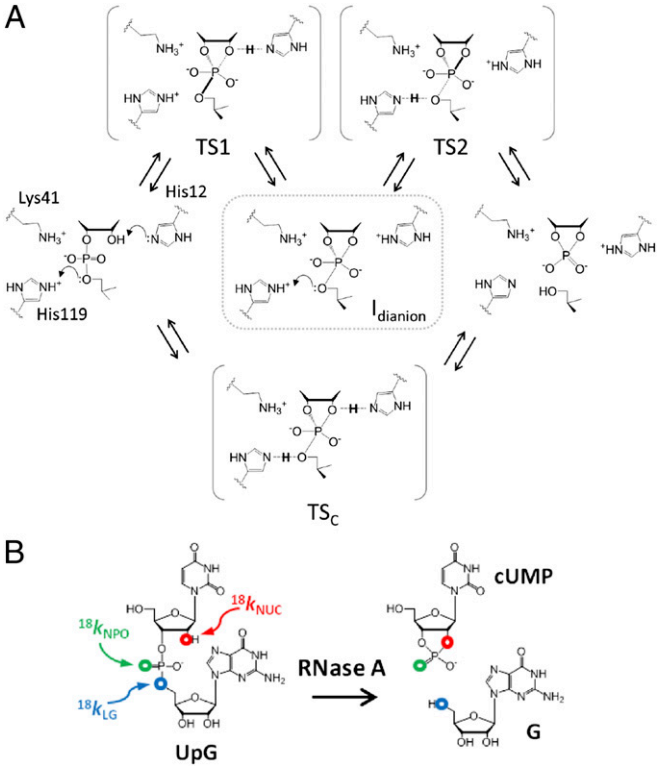


**Fig. 1.** (*A*) Proposed active site interactions and potential transition states for RNase A. A concerted mechanism with simultaneous nucleophilic attack, leaving group departure, and concomitant proton transfer involving both His12 and His119 is shown in the lowest pathway. The most likely stepwise mechanism involves nucleophilic attack (via TS1) and leaving group departure (via TS2) separated by a dianionic intermediate that may be only short-lived. (*B*) RNA dinucleotide substrate (UpG) reacts via 2′-*O*-transesterification to yield 2′,3′-cyclic uridine monophosphate (cUMP) and guanosine (G) products. Sites of isotopic substitution used to measure the KIEs for the $^{18}k_{NUC}$, $^{18}k_{NPO}$, and 5′O $^{18}k_{LG}$ are indicated in red, green, and blue, respectively.

a role in leaving group stabilization (7). However, the more highly reactive *p*-nitrophenol leaving group may result in a change in mechanism compared with the less reactive ribose 5′O, making it difficult to interpret these results without an understanding of the mechanism and rate-limiting transition state. Substitution of His12 and His119 with 4-fluorohistidine ($pK_a = 3.5$) changes the apparent macroscopic $pK_a$ values determined from analysis of the pH dependence of $k_{cat}/K_m$ with their proposed roles in acid/base catalysis (11). However, effects of 4-fluorohistidine substitution on catalysis are only *ca*. 10-fold, suggesting a relatively small Brønsted effect, or that a nonchemical step is partially rate-limiting. Thus, even for this well-studied enzyme, significant ambiguity remains regarding the interactions with the transition state that provide catalysis.

A powerful method to gain insight into mechanism and transition state structure is to determine the KIEs on substrate atoms and to use the results as benchmarks for evaluating computational simulations (12, 13). The effects of stable heavy atom isotope substitution on reaction rate constants arise mainly due to differences in vibrational zero point energies, and their magnitudes provide information on the differences in bonding between the ground state and transition state (14, 15). Leaving group and NPO KIEs for RNase A cleavage of uridine-*m*-nitrobenzyl phosphate were previously reported by Cleland and colleagues (16). However, this study lacked information on nucleophile bonding and involved a model substrate that lacks binding interactions present in authentic RNA substrates.

Here, KIE measurements on enzyme and solution RNA reactions are coordinated with MD simulations and quantum mechanical (QM) calculations to achieve a detailed model of the transition state for enzymatic RNA cleavage. Together, the results reveal a transition state with advanced 2′O-P bond formation and 5′O-P bond cleavage similar to the late anionic transition state for solution reactions catalyzed by a specific base. MD simulations are consistent with protonated His12 and Lys41 stabilizing an anionic, phosphorane-like transition state by H-bonding to the phosphoryl oxygens, whereas protonated His119 is poised to transfer a proton to the 5′O leaving group. Importantly, the KIEs for the RNase A reaction reveal a significant difference in 5′O bonding compared with solution reactions. Supported by QM calculations, we ascribe this difference to less advanced P-O bond cleavage and proton transfer (general acid catalysis) from His119.

## Results and Discussion

**Measurement of $^{18}$O KIEs on RNA 2′-*O*-Transphosphorylation Reactions.** KIEs are typically measured by competitive methods (12) in which mixtures of substrates containing either $^{16}$O or $^{18}$O at one of the reactive phosphoryl oxygens are analyzed (Fig. 1*B*). The larger rate constant for either the $^{18}$O- or $^{16}$O-containing RNA results in progressive depletion of that isotopologue in the unreacted substrate population. Quantitative analysis of the $^{18}$O/$^{16}$O ratio as a function of reaction progress allows calculation of the KIE, which is expressed as the ratio of the rate constants for the light and heavy isotopologues ($^{18}k = k_{16}/k_{18}$) (12). KIEs reflect both the extent to which the labeled atom participates in the reaction coordinate and differences in vibrations of the labeled atom in the ground state compared with the transition state (14). Bond breakage, or a "looser" bonding environment in the transition state relative to the ground state results in faster reactivity for the light isotopologue, and thus an $^{18}k$ that is greater than unity (referred to as a normal KIE). Conversely, bond formation or a "stiffer" bonding environment favors the heavier isotopologue, and the observed KIE is less than unity (referred to as an inverse KIE). The fractionation of $^{18}$O will also depend on proton transfer in both preequilibrium and chemical steps (12), and may offset the contributions of O-P bonding. Additionally, both bonding and bending vibrational modes can influence the observed KIE on the nonbridging oxygens, and these effects may also be offsetting (13). Deciphering the relative contributions of proton transfer, O-P bonding, and other vibrational modes can be difficult; however, the magnitude of observed KIEs provides insight into mechanism and transition state bonding unobtainable by any other means.

Substrate RNA dinucleotides enriched with $^{18}$O at the 2′O, 5′O, and NPO positions were synthesized (Fig. 1*B*) and reacted with acid and base and with RNase A. The fraction of reaction was measured by integration of RP-HPLC chromatograms in which the $^{18}$O/$^{16}$O ratio was determined by MS (6) (*SI Text* and

**Table 1. Comparison of $^{18}k_{LG}$, $^{18}k_{NUC}$, and $^{18}k_{NPO}$ KIE values for 2′-*O*-transphosphorylation catalyzed by acid, base, and RNase A**

| Catalyst | $^{18}k_{LG}$ | $^{18}k_{NUC}$ | $^{18}k_{NPO}$ |
|---|---|---|---|
| RNase A, pH 7 | 1.014(3) | 0.994(2) | 1.001(1) |
| RNase A (QM) | 1.026 | 0.998 | 1.006 |
| Acid, pH 0 | 1.005(4) | 0.990(4) | 0.991(1) |
| Base, pH 12 (7, 8) | 1.037(2) | 0.996(2) | 0.999(1) |
| Base, pH 14 (8) | 1.034(4) | 0.984(3) | — |
| Base, pH 14 (QM) | 1.046 | 0.973 | 1.002 |

SDs for measured KIEs are shown in parentheses (*Methods*).

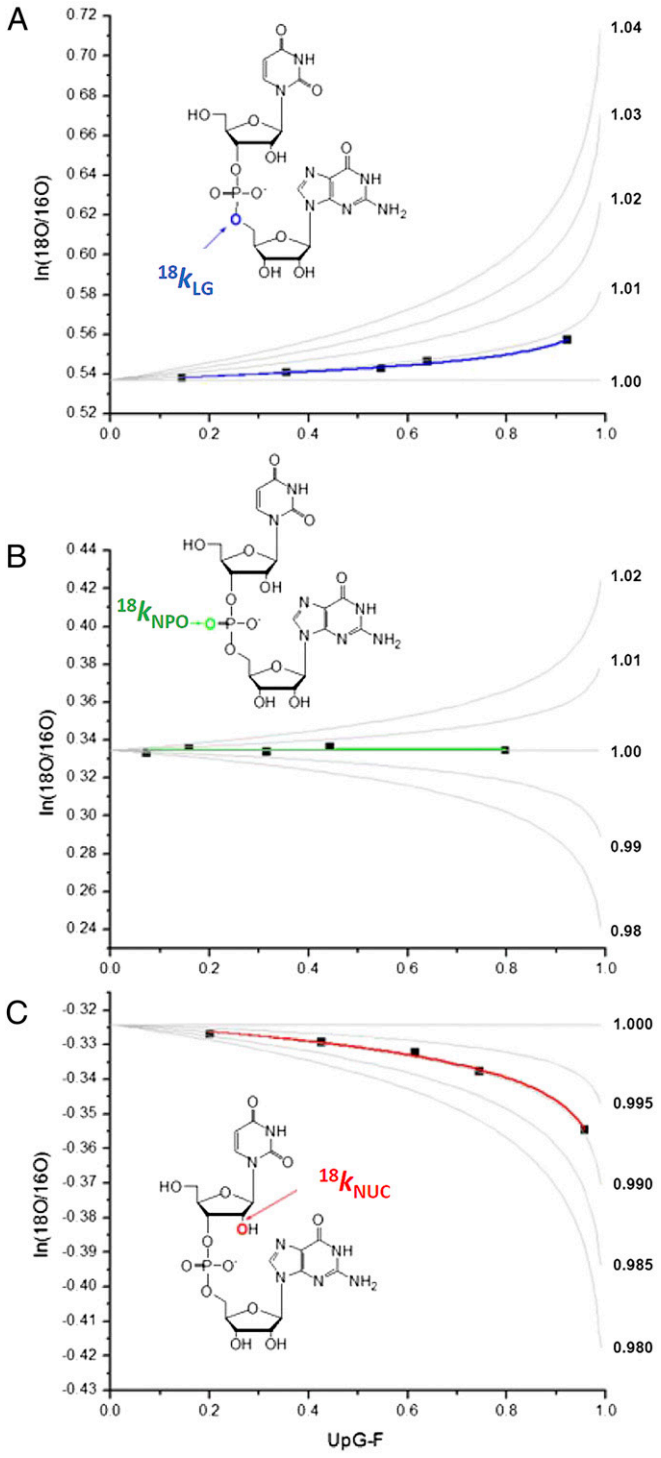


**Fig. 2.** Determination of KIEs for RNase A-catalyzed RNA 2′-*O*-transphosphorylation by analysis of the change in the $^{18}O/^{16}O$ ratio ($\ln {}^{18}O/{}^{16}O$) as a function of reaction progress (F). The $^{18}O/^{16}O$ ratio determined by MS is plotted relative to reaction progress, and the data are fit as described in *Methods*. Example fits of data used to calculate the $^{18}k_{LG}$ (*A*), $^{18}k_{NPO}$ (*B*), and $^{18}k_{NUC}$ (*C*) are shown. Experimental data points are shown as filled squares. Simulations for curves representing a range of potential KIEs are shown as gray lines.

Fig. S2*A*). Two product ions contain the isotopically enriched positions: a species at *m/z* 476/478 resulting from loss of the uridine base and a 211/213 fragment composed of ribose phosphate (Fig. S2*B*). The KIE is observed as a change in the relative ratios of the product ions containing only $^{16}O$ at all oxygens (M) and those containing $^{18}O$ at one of the reacting phosphoryl oxygens (M + 2) (Fig. S2*C*). Fig. 2 shows the determination of KIEs for RNase A-catalyzed 2′-*O*-transphosphorylation of uridylyl-3′-guanosine [5′-UpG-3′ (UpG)] relative to simulations of $^{18}O/^{16}O$ ratio vs. *F* (the fraction of substrate UpG reacted to form a product) for a range of potential $^{18}O$ KIEs.

**Transition States of Solution Reactions Catalyzed by Acid and Base.** The nucleophile ($^{18}k_{NUC}$), leaving group ($^{18}k_{LG}$), and NPO ($^{18}k_{NPO}$) KIE results presented in Table 1 for acid- and base-catalyzed 2′-*O*-transphosphorylation reactions of UpG, together with previous biophysical and biochemical studies, provide a framework for understanding the RNase A transition state. For solution 2′-*O*-transphosphorylation, previous experimental and computational data are consistent with the observed $^{18}k_{NUC}$ being a combination of normal contributions from deprotonation and an inverse effect from advanced 2′O-P bond formation (6, 17). Together, these contributions result in the inverse values observed for the stepwise acid-catalyzed reaction (pH 0) and a similar inverse $^{18}k_{NUC}$ for the late anionic transition state for base catalysis (pH 12) [0.990(4) and 0.996(2), respectively, with standard deviations in parentheses] (6, 18–20). These data are consistent with analyses of nucleophile bonding by LFERs of RNA reactions catalyzed by a specific base, which show that the 2′ oxyanion formed in a preequilibrium deprotonation step undergoes substantial loss of negative charge in the transition state (21).

The observed $^{18}k_{NPO}$ is an average of the KIEs on the two NPOs because only one of the two positions is enriched nonspecifically (20). Nonetheless, a late TS2 for the base-catalyzed reaction is further indicated by a near-unity $^{18}k_{NPO}$, which indicates a similar bonding environment in the transition state and in the ground state monoanion. In contrast, formation of a protonated phosphorane during acid catalysis is consistent with the observed inverse $^{18}k_{NPO}$ [0.991(1)] as previously reported for acid catalysis of uridine-3′*m*-nitrobenzyl phosphate transphosphorylation (22).

The $^{18}k_{LG}$ for acid catalysis is small [1.005(4)], consistent with models that propose rate-limiting phosphorane breakdown with concomitant transfer of a proton from a phosphoryl oxygen to the 5′O (22) (Fig. S1*A*). Base-catalyzed RNA 2′-*O*-transphosphorylation is sensitive to the $pK_a$ of the leaving group, with a $\beta_{LG}$ of −1.28 indicating that the alkoxide character of the 5′O is advanced (23), which is consistent with the observed large normal $^{18}k_{LG}$ value [1.037(2)]. This value is near the expected maximum (*ca.* 1.04) for breakage of an O-P bond (13). Recent QM simulations of the base-catalyzed reaction identify a representative late transition state for breakdown of a transient dianionic phosphorane ($TS2_B$ in Fig. S1*C*) that reproduces the observed inverse $^{18}k_{NUC}$, large normal $^{18}k_{LG}$, and near-unity $^{18}k_{NPO}$ (6, 20). For a rate-limiting TS1, a normal $^{18}k_{NUC}$ and a small normal $^{18}k_{LG}$ are predicted (20). For a concerted mechanism a less inverse $^{18}k_{NUC}$, as well as a normal or inverse $^{18}k_{NPO}$, is observed depending on the associative or dissociative character of $TS_c$ (2, 17, 24).

**RNase A Kinetics and Substrate Binding Commitments.** KIEs measured by competitive methods are effects on $k_{cat}/K_m$; therefore, substrate binding steps may interfere with the KIE measurements for RNase A. If substrate dissociation is slow relative to chemistry, resulting in a "commitment" of the bound substrate to undergo chemical transformation, the commitment generates an attenuation of the observed KIEs relative to their intrinsic values (12). Several lines of evidence support the assertion that observed KIEs on the RNase A reaction approximate intrinsic effects on the chemical step (*SI Text*). Foremost, the KIEs for

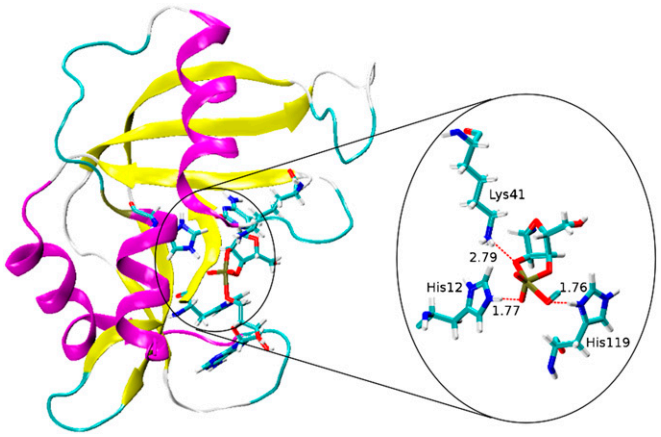


**Fig. 3.** Structure of RNase A transition state mimic derived from a 50-ns MD simulation using the assisted model building with energy refinement (AMBER) FF10 force field in TIP4PEw water (1-ns average). The dianionic transition state is stabilized by interactions between His12, Lys41, and His119 and the transition state. In this model, His119 is poised for general acid catalysis, whereas His12, in its protonated form (after accepting a proton from the nucleophile), provides electrostatic stabilization to the transition state.

RNase A in Table 1 are nonzero, indicating that the chemical step is at least partially rate-limiting (6, 22). The leaving group KIE for RNase A is similar to the value measured by Cleland and colleagues (16) for the slow model substrate uridine-3′-*m*-nitrobenzyl phosphate. UpG is also a slow substrate with *ca*. 40-fold lower $k_{cat}/K_m$ compared with an optimal uridylyl-3′-adenosine [5′-UpA-3′ (UpA)] dinucleotide substrate (Fig. S3). The $k_{cat}/K_m$ for UpG is similar in magnitude to that for uridine 3′-*p*-nitrophenol phosphate substrate, which has been argued to react with a rate-limiting step subsequent to binding based on lack of sensitivity to solvent viscosity (25). The rate of UpG cleavage by RNase A under $k_{cat}/K_m$ conditions is also insensitive to viscosity (Fig. S4). The pH dependence of $k_{cat}/K_m$ for the reaction of the UpG (Fig. S5) is bell-shaped, as expected, and shows apparent macroscopic $pK_a$ values ($5.2 \pm 0.2$ and $6.3 \pm 0.1$) that are similar to the microscopic $pK_a$ values of His12 and His119 determined by NMR (5.7 and 6.3) (26), which is also consistent with minimal binding commitments under conditions where KIEs were measured.

**KIE Analysis of RNase A-Catalyzed RNA 2′-*O*-Transesterification.** The inverse $^{18}k_{NUC}$ [0.994(2)] for RNase A suggests that 2′O-P bond formation is advanced in the rate-limiting transition state. A similar inverse $^{18}k_{NUC}$ is observed for the stepwise mechanism for acid catalysis in which the phosphorane is sufficiently stable to undergo pseudorotation (Table 1). The base-catalyzed solution reaction also has an inverse $^{18}k_{NUC}$ [0.996(2)], which becomes more inverse [0.984(3)] above the $pK_a$ of the 2′OH consistent with loss of the contribution from 2′O deprotonation (6). QM simulations of the base-catalyzed reaction that are consistent with the KIE data indicate a late anionic transition state (TS2 in Fig. S1) and suggest the formation of a transient dianionic phosphorane (20, 27). Interpretation of advanced 2′O-P bonding in the RNase A transition state assumes that the measured $^{18}k_{NUC}$ includes a large inverse contribution 2′O-P bonding that is partially offset by a normal equilibrium isotope effect (EIE) from alcohol deprotonation (28). The relative magnitudes of these contributions are difficult to assess, and combinations of less advanced 2′O-P bonding and partial proton transfer in the transition state (general base catalysis) cannot be entirely excluded.

The small $^{18}k_{NPO}$ for the RNase A reaction indicates that the NPOs experience a similar bonding environment in both the ground state and transition state, which is also consistent with a late product-like transition state. An $^{18}k_{NPO}$ near unity is inconsistent with protonation of an NPO. In this case, an inverse $^{18}k_{NPO}$ would be predicted similar to that observed for acid catalysis [0.991(1)]. Together with the lack of a thio effect on RNase A (10), these results provide strong evidence against protonation. Rather, the small normal $^{18}k_{NPO}$ we observe suggests that the NPO atoms gain anionic character in the transition state.

The normal $^{18}k_{LG}$ for RNase A indicates breaking of the 5′O-P bond in the rate-limiting transition state similar to catalysis by a specific base in solution (6). However, the $^{18}k_{LG}$ for the enzyme reaction is significantly less than the value observed for the solution reaction [1.014(3) vs. 1.037(2)], indicating a stiffer bonding environment for the 5′O in the enzyme active site. Alternatively, the smaller $^{18}k_{LG}$ for RNase A could result from a small binding commitment, although available experimental evidence suggests this is unlikely (*SI Text*). In this case, the intrinsic $^{18}k_{NUC}$ would be more inverse than the solution reaction, which seems unlikely because the measured value of *ca*. 0.994 is already characteristic of advanced 2′O-P bonding. The predicted large normal $^{18}k_{LG}$ would indicate advanced 5′O-P bond cleavage with a minimal effect of enzyme interactions in mitigating the unfavorable accumulation of negative charge. If the effects accurately reflect intrinsic KIEs on the chemical step, the difference in $^{18}k_{LG}$ could reflect less 5′O-P bond cleavage in the RNase A transition state. It is likely that proton transfer to the 5′O would result in a stiffer bonding environment, given the large inverse EIE in the direction of deprotonation of *ca*. 0.976 (28) and the proximity of His119.

**MD Simulations and QM Calculations to Model the Mechanism and Transition State.** To gain further insight into the mechanistic implications of the KIE measurements, we performed MD simulations and QM calculations that build on previous work for RNase A (9) and nonenzymatic models (20, 27). Based on the KIE results supporting an anionic transition state with advanced 2′O-P bonding, we first performed MD simulations of RNase A with a dianionic phosphorane transition state mimic as described previously (9). Because transfer of the 2′ proton is considered to be complete in this model, His12 and His119 are protonated to characterize the electrostatic stabilization of the anionic transition state. The results summarized in Fig. 3 are derived from a 50-ns MD simulation and suggest that a protonated His12, formed in the general base step of a stepwise mechanism, can further provide electrostatic stabilization of an anionic phosphorane intermediate/transition state. Throughout the simulation, the imidazolium side chain of His119 forms a strong hydrogen bond with

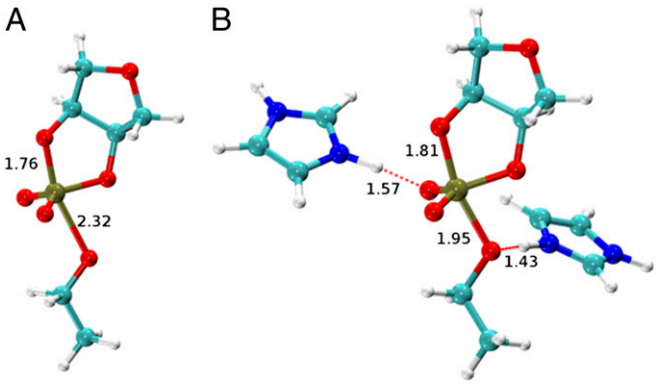


**Fig. 4.** Transition state structures for the nonenzymatic dianionic transition state model for the specific base reaction (*A*) and for the enzymatic transition state model based on hydrogen bonding in the active site of the RNase A (*B*).

the 5′O (Fig. 3). Our findings suggest that RNase A can support a mechanism involving a transient anionic phosphorane intermediate or phosphorane-like transition state like the one implicated by theoretical and experimental studies of specific base catalysis (20, 27). Moreover, the MD results provide a basis for construction of a fully QM active site model from which transition state structures can be determined and KIEs can be estimated.

KIEs were calculated for both enzymatic and nonenzymatic reaction models using density-functional theory and a continuum model to treat solvation effects (*Methods*). The nonenzymatic model corresponds to alkaline conditions and assumes that the deprotonation of the 2′OH occurs in a prior step that is not rate-controlling. In the enzymatic model, the 2′OH is assumed to be protontated in the ground state; however, whether deprotonation occurs in a preequilibrium step or concomitant with nucleophilic attack is not known. The enzymatic reaction model was based on the MD simulation structures and consisted of the hypothesized dianionic phosphorane stabilized by hydrogen bonds donated from two histidine side chains (protonated imidazoles). Results for the nonenzymatic reaction model were similar to our previous results using an ethylene glycol phosphate methyl ester (20, 27) in which nucleophile bonding is advanced (1.8 Å compared with 1.7 Å for an O-P bond). Here, we included a more realistic ribose-like sugar ring and ethoxide leaving group, and obtained KIE results in better agreement with experimental data (Fig. 4 and Table 1). Comparison of the calculated KIEs for the nonenzymatic QM model with the measured values for the solution reaction catalyzed by a specific base (calculated/measured) reveal an inverse $^{18}k_{NUC}$ (0.973/0.984), large normal $^{18}k_{LG}$ (1.046/1.034), and near-unity $^{18}k_{NPO}$ (1.002/0.999).

Alternative mechanistic models involving protonation of an NPO or the 5′O alone and 5′O protonation in the presence of H-bonding to an NPO were evaluated (Table S1 and Fig. S6). The calculated and measured KIE values are in good agreement for the enzymatic reaction model involving proton transfer from His119 to the 5′O, together with H-bonding between the active site and the NPO atoms [$^{18}k_{NUC}$ (0.998/0.994), $^{18}k_{LG}$ (1.026/1.014), and $^{18}k_{NPO}$ (1.006/1.001) (calculated/measured)] (Table 1). Importantly, the calculated $^{18}k_{LG}$ for the base-catalyzed reaction simulation (1.048) is notably larger than the calculated $^{18}k_{LG}$ for the enzymatic model (1.026), consistent with the observed experimental trend (1.034 vs. 1.017). In the simulations, the P-5′O bond length is considerably shorter for the RNase A transition state than that for the base-catalyzed reaction (1.95 Å vs. 2.3 Å) (Fig. 4) and it retains a higher degree of covalent bond character. Moreover, proton transfer from the general acid (His119) further creates a stiffer bonding environment for stabilizing the leaving group.

The results reported here are comparable to those of previous studies directed at determining the influence of active site environments on transition state structure. Herschlag and colleagues (29, 30) reported a large negative $\beta_{LG}$, as well as a large leaving group KIE for both alkaline phosphatase (AP) and nonenzymatic monoester hydrolysis. These results are consistent with a dissociative transition state both on and off the enzyme. However, a more inverse nonbridging oxygen KIE is observed for AP and is consistent with active site metal coordination in the transition state (29). In solution, acid-catalyzed hydrolysis of nucleoside glycosidic bonds occurs via dissociative transition states with considerable oxycarbonium ion character in the ribose ring (31, 32). Human and malarial purine nucleoside phosphorylases proceed through similarly dissociative transition states (33); however, more associative transition states are observed for $NAD^+$ hydrolysis by both diphtheria toxin and human thymidine phosphorylase (34, 35). Nonenzymatic peptide bond formation occurs with equilibrium deprotonation and nucleophilic attack of a neutral amine and loss of a second proton from nitrogen on breakdown of a zwitterionic intermediate (36). Recent KIE and computational results by Hiller et al. (37) suggest that in the ribosome active site, the second deprotonation occurs concomitant with C-N bond formation. These examples illustrate that interactions with enzyme active site residues can subtly alter the transition state in a manner reflecting, in part, the nature of catalytic modes that are used.

In the present study, coordinated theory and experiment provide a chemically detailed comparison of transition state structures for RNA 2′-*O*-transphosphorylation in solution and in the active site of RNase A. The results reveal that both reactions can proceed via late anionic transition states with complete loss of the 2′O proton and advanced 2′O-P bonding. Nonetheless, the active site environment provides a combination of interactions (general acid and electrostatic catalysis), and thereby influences transition state structure. Electrostatic interactions with positively charged amino acid site chains (His12/Lys41), together with proton transfer from His119, render departure of the 5′O less advanced compared with the solution reaction and stabilize charge buildup in the transition state. Expulsion of the 5′O remains an integral feature of the rate-limiting step both on and off the enzyme, reflecting principles that are fundamental to RNA 2′-*O*-transphosphorylation reactions. In addition to mechanistic insights, the transition state structure reported here could aid inhibitor design through the construction of stable molecules that mimic its charge distribution. The ability to obtain a chemically detailed description of 2′-*O*-transphosphorylation transition states paves the way for a new frontier in understanding biological catalysis: defining how active site environments of phosphoryl transferases and substrate reactivity influence transition state structure.

## Methods

**Determination of $^{18}$O KIEs on RNA 2′-*O*-Transphosphorylation Reactions.** The reaction kinetics and KIEs on the $^{18}k_{NUC}$, $^{18}k_{LG}$, and $^{18}k_{NPO}$ for UpG to form 2′,3′-cyclic uridine monophosphate and guanosine were analyzed essentially as described by Harris et al. (6) (*SI Text* and Fig. S2*B*). Briefly, KIEs were determined by analyzing the change in the $^{16}O/^{18}O$ ratio of an RNA substrate of defined sequence that has been site-specifically enriched with $^{18}$O at the 2′O, 5′O (6, 20, 38), or NPO position as a function of reaction progress. The KIE values determined in Fig. 2 and reported in Table 1 were calculated from plots of $\ln(^{18}O/^{16}O)$ vs. $F$ by fitting to $\ln(^{18}O/^{16}O) = (1/^{18}k - 1)\ln(1 - F) + \ln(R_0)$, where $^{18}k$ is the isotope effect, $F$ is the fraction of substrate consumed as determined from integration of HPLC chromatograms, and $R_0$ is the initial $^{18}O/^{16}O$ ratio in the unreacted substrate. Fitting errors and comparison of fits of the data to the equation, above, to simulations at different isotope effects at the same $R_0$ in Fig. 2 show the precision to be in the range of 0.2–0.5%.

**MD Simulation and QM Calculation Methods.** Isothermal-isobaric (300 K, 1 atm) MD simulations of RNase A bound to a dinucleotide cytidylyl-3′-adenosine [5′-CpA-3′ (CpA)] having the 3′,5′-phosphodiester linkage replaced by a pentacovalent phosphorane 2′-*O*-transphosphorylation transition-state mimic (Fig. 3) were performed for 50 ns, starting from the X-ray crystal structure complexed with cytidilyl-3′-5′-adenosine (Protein Data Bank ID code 1RPG) (39). His12, His119, and Lys41 were in their protonated (+1) states. The assisted model building with energy refinement (AMBER) FF10 force field (40) was used to describe the RNase A protein, along with a set of specific force-field parameters to mimic the late transition state of the dinucleotide (41) and the TIP4PEw model for water (42). The software not (just) another molecular dynamics program (NAMD) was used for all MD simulations (43). For the QM calculations on the nonenzymatic and enzymatic models (Fig. 4), the structures of reactants and the transition states in solution were obtained through full geometry optimization using density-functional theory with solvation effects included through the polarizable continuum model (44) and with specialized atomic radii and smooth analytical gradients for treating the solvent effects (45–48). The hybrid B3LYP exchange-correlation functional was used together with the 6–31++G(d,p) basis set. Vibrational frequency analyses were performed to confirm the nature of all stationary points (minima and transition states). KIEs were then calculated from the Bigeleisen equation (14) at 37 °C based on the density functional theory (DFT) potential energy surface. The software package Gaussian 09 was used for all QM calculations (49).

**ACKNOWLEDGMENTS.** We gratefully acknowledge the encouragement, advice, and seminal contributions of Dr. W. W. Cleland. We thank Dr. Dan Herschlag for providing advice on mechanistic interpretations and comments on the manuscript. This work was supported by the Case Western Reserve University Center for Proteomics and Bioinformatics Center and by National Institutes of Health (NIH) Grant GM096000 (to M.E.H.), NIH Grant AI081987 (to J.A.P.), Hong Kong Baptist University (HKBU) startup and Faculty Research Grant funds (38-40-088 and 40-49-495) to K.-Y.W., and NIH Grant GM064288 (to D.M.Y.). D.L.K. was supported by NIH Training Grant T32-GM008056. This work was partially supported by the computing resources of the Minnesota Supercomputing Institute, by the High Performance Cluster Computing Centre and the Information Technology Office at HKBU (sciblade and jiraiya), and by the National Science Foundation through TeraGrid resources provided by Ranger, Texas Advanced Computing Center, and Kraken at the National Institute for Computational Sciences under Grant TG-CHE100072.

1. Jencks WP (1969) *Catalysis in Chemistry and Enzymology*, McGraw–Hill Series in Advanced Chemistry (McGraw–Hill, New York).
2. Cleland WW, Hengge AC (1995) Mechanisms of phosphoryl and acyl transfer. *FASEB J* 9(15):1585–1594.
3. Lassila JK, Zalatan JG, Herschlag D (2011) Biological phosphoryl-transfer reactions: Understanding mechanism and catalysis. *Annu Rev Biochem* 80:669–702.
4. Perreault DM, Anslyn EV (1997) Unifying the current data on the mechanism of cleavage—Transesterification of RNA. *Angew Chem Int Ed Engl* 36(5):432–450.
5. Oivanen M, Kuusela S, Lönnberg H (1998) Kinetics and mechanism for the cleavage and isomerization of phosphodiester bonds of RNA by Bronsted acids and bases. *Chem Rev* 98(3):961–990.
6. Harris ME, et al. (2010) Kinetic isotope effects for RNA cleavage by 2′-O- transphosphorylation: Nucleophilic activation by specific base. *J Am Chem Soc* 132(33): 11613–11621.
7. Raines RT (1998) Ribonuclease A. *Chem Rev* 98(3):1045–1066.
8. Elsässer B, Valiev M, Weare JH (2009) A dianionic phosphorane intermediate and transition states in an associative A(N)+D(N) mechanism for the ribonucleaseA hydrolysis reaction. *J Am Chem Soc* 131(11):3869–3871.
9. Formoso E, Matxain JM, Lopez X, York DM (2010) Molecular dynamics simulation of bovine pancreatic ribonuclease A-CpA and transition state-like complexes. *J Phys Chem B* 114(21):7371–7382.
10. Herschlag D (1994) Ribonuclease revisited: Catalysis via the classical general acid-base mechanism or a triester-like mechanism? *J Am Chem Soc* 116(26):11631–11635.
11. Jackson DY, et al. (1994) A designed peptide ligase for total synthesis of ribonuclease A with unnatural catalytic residues. *Science* 266(5183):243–247.
12. Cleland WW (2005) The use of isotope effects to determine enzyme mechanisms. *Arch Biochem Biophys* 433(1):2–12.
13. Hengge AC (2002) Isotope effects in the study of phosphoryl and sulfuryl transfer reactions. *Acc Chem Res* 35(2):105–112.
14. Bigeleisen J, Wolfsberg M (1958) Theoretical and experimental aspects of isotope effects in chemical kinetics. *Adv Chem Phys* 1(1):15–76.
15. O'Leary MH (1977) Studies of enzyme reaction mechanisms by means of heavy atom isotope effects. *Isotope Effects on Enzyme Catalyzed Reactions*, eds Cleland WW, O'Leary MH, Northrop DB (University Park Press, Baltimore), pp 233–251.
16. Sowa GA, Hengge AC, Cleland WW (1997) 18O isotope effects support a concerted mechanism for ribonuclease A. *J Am Chem Soc* 119:2319–2320.
17. Humphry T, et al. (2008) Altered transition state for the reaction of an RNA model catalyzed by a dinuclear zinc(II) catalyst. *J Am Chem Soc* 130(52):17858–17866.
18. Humphry T, Forconi M, Williams NH, Hengge AC (2004) Altered mechanisms of reactions of phosphate esters bridging a dinuclear metal center. *J Am Chem Soc* 126 (38):11864–11869.
19. Cassano AG, Anderson VE, Harris ME (2002) Evidence for direct attack by hydroxide in phosphodiester hydrolysis. *J Am Chem Soc* 124(37):10964–10965.
20. Wong KY, et al. (2012) Characterization of the reaction path and transition states for RNA transphosphorylation models from theory and experiment. *Angew Chem Int Ed Engl* 51(3):647–651.
21. Ye JD, Li NS, Dai Q, Piccirilli JA (2007) The mechanism of RNA strand scission: An experimental measure of the Brønsted coefficient, beta nuc. *Angew Chem Int Ed Engl* 46(20):3714–3717.
22. Gerratana B, Sowa GA, Cleland WW (2000) Characterization of the transition state structures and mechanisms for the isomerization and cleavage reactions of 3′-m-nitrobenzyl phosphate. *J Am Chem Soc* 122(51):12615–12621.
23. Lonnberg H, Stromberg R, Williams A (2004) Compelling evidence for a stepwise mechanism of the alkaline cyclisation of uridine 3′-phosphate esters. *Org Biomol Chem* 2(15):2165–2167.
24. Cleland WW (1990) Secondary 18O isotope effects as a tool for studying reactions of phosphate mono-, di-, and triesters. *FASEB J* 4(11):2899–2905.
25. Thompson JE, et al. (1995) Limits to Catalysis by Ribonuclease A. *Bioorg Chem* 23(4): 471–481.
26. Quirk DJ, Park C, Thompson JE, Raines RT (1998) His...Asp catalytic dyad of ribonuclease A: Conformational stability of the wild-type, D121N, D121A, and H119A enzymes. *Biochemistry* 37(51):17958–17964.
27. Radak BK, Harris ME, York DM (2013) Molecular simulations of RNA 2′-O-transesterification reaction models in solution. *J Phys Chem B* 117(1):94–103.
28. Rishavy MA, Cleland WW (1999) 13C, 15N and 18O equilibrium isotope effects and fractionation factors. *Can J Chem* 77(5-6):967–977.
29. Zalatan JG, et al. (2007) Kinetic isotope effects for alkaline phosphatase reactions: Implications for the role of active-site metal ions in catalysis. *J Am Chem Soc* 129(31): 9789–9798.
30. Catrina I, et al. (2007) Probing the origin of the compromised catalysis of E. coli alkaline phosphatase in its promiscuous sulfatase reaction. *J Am Chem Soc* 129(17): 5760–5765.
31. Mentch F, Parkin DW, Schramm VL (1987) Transition-state structures for N-glycoside hydrolysis of AMP by acid and by AMP nucleosidase in the presence and absence of allosteric activator. *Biochemistry* 26(3):921–930.
32. Berti PJ, Schramm VL (1997) Transition State Structure of the Solvolytic Hydrolysis of $NAD^+$. *J Am Chem Soc* 119(50):12069–12078.
33. Taylor Ringia EA, Schramm VL (2005) Transition states and inhibitors of the purine nucleoside phosphorylase family. *Curr Top Med Chem* 5(13):1237–1258.
34. Berti PJ, Blanke SR, Schramm VL (1997) Transition State Structure for the Hydrolysis of NAD Catalyzed by Diphtheria Toxin. *J Am Chem Soc* 119(50):12079–12088.
35. Schwartz PA, Vetticatt MJ, Schramm VL (2010) Transition state analysis of thymidine hydrolysis by human thymidine phosphorylase. *J Am Chem Soc* 132(38):13425–13433.
36. Leung EK, Suslov N, Tuttle N, Sengupta R, Piccirilli JA (2011) The mechanism of peptidyl transfer catalysis by the ribosome. *Annu Rev Biochem* 80:527–555.
37. Hiller DA, Singh V, Zhong M, Strobel SA (2011) A two-step chemical mechanism for ribosome-catalysed peptide bond formation. *Nature* 476(7359):236–239.
38. Dai Q, Frederiksen JK, Anderson VE, Harris ME, Piccirilli JA (2008) Efficient synthesis of [2′-18O]uridine and its incorporation into oligonucleotides: A new tool for mechanistic study of nucleotidyl transfer reactions by isotope effect analysis. *J Org Chem* 73 (1):309–311.
39. Zegers I, et al. (1994) The structures of RNase A complexed with 3′-CMP and d(CpA): Active site conformation and conserved water molecules. *Protein Sci* 3(12):2322–2339.
40. Hornak V, et al. (2006) Comparison of multiple Amber force fields and development of improved protein backbone parameters. *Proteins* 65(3):712–725.
41. Lee TS, Giambaşu G, Harris ME, York DM (2011) Characterization of the Structure and Dynamics of the HDV Ribozyme at Different Stages Along the Reaction Path. *J Phys Chem Lett* 2(20):2538–2543.
42. Horn HW, et al. (2004) Development of an improved four-site water model for biomolecular simulations: TIP4P-Ew. *J Chem Phys* 120(20):9665–9678.
43. Phillips JC, et al. (2005) Scalable molecular dynamics with NAMD. *J Comput Chem* 26 (16):1781–1802.
44. Cossi M, Rega N, Scalmani G, Barone V (2003) Energies, structures, and electronic properties of molecules in solution with the C-PCM solvation model. *J Comput Chem* 24(6):669–681.
45. Khandogin J, Gregersen BA, Thiel W, York DM (2005) Smooth solvation method for d-orbital semiempirical calculations of biological reactions. 1. Implementation. *J Phys Chem B* 109(19):9799–9809.
46. Scalmani G, Frisch MJ (2010) Continuous surface charge polarizable continuum models of solvation. I. General formalism. *J Chem Phys* 132(11):114110.
47. York DM, Karplus M (1999) A smooth solvation potential based on the conductor-like screening model. *J Phys Chem A* 103(50):11060–11079.
48. Gregersen BA, York DM (2005) High-order discretization schemes for biochemical applications of boundary element solvation and variational electrostatic projection methods. *J Chem Phys* 122(19):194110.
49. Frisch MJ, et al. (2009) *Gaussian 09, Revision B.01* (Wallingford, CT). Available at www.gaussian.com. Accessed July 9, 2013.

# Supporting Information

Gu et al. 10.1073/pnas.1215086110

## SI Text

**Determination of Kinetic Isotope Effects on RNA 2′-*O*-Transphosphorylation Reactions.** Solution and enzyme kinetic isotope effects (KIEs) were measured for the 2′-*O*-transphosphorylation reaction of the dinucleotide uridylyl-(3′,5′)-guanosine (5′-UpG-3′ or UpG) (Fig. 1*B*) to form 2′,3′-cyclic uridine monophosphate (cUMP) and guanosine (G). UpG was synthesized to contain $^{18}O$ at the 2′O, 5′O, and nonbridging phosphoryl oxygen (NPO) positions, individually. Briefly, the $^{18}O$-enriched RNA was synthesized using [$^{18}O_2$]benzoic acid as a nucleophile to deliver the isotopic substitution to activated nucleoside ribose 2′ or 5′ carbons of protected ribonucleosides, followed by hydrolysis of the benzoate ester as described. The [2′-$^{18}O$]- or [5′-$^{18}O$]-nucleoside was coupled to commercially available phosphoramidite to yield the RNA dinucleotides [2′-$^{18}O$]UpG and Up-[5′-$^{18}O$]G. Up[NPO-$^{18}O$]G was synthesized by including $H_2{}^{18}O$ in the hydrolysis step during solid phase synthesis (1).

The 2′-*O*-transphosphorylation reaction of UpG catalyzed by specific base was performed as described, and catalysis by specific acid was analyzed similarly (2). Briefly, the reaction of 1–5 nmol of UpG at pH 0 (1 M HCl) was carried out in 250–500 μL at 37 °C. Kinetics were followed by removing aliquots at specific times and neutralizing with an equivalent of NaOH, followed by further dilution with 100–200 μL of 0.1 M ammonium acetate at pH 8.0. For RNase A reactions, the enzyme was removed by centrifugation through Centricon-10 filters (Millipore) and the flow-through was collected.

The reactant (UpG) and products (cUMP and G) were resolved by RP-HPLC on a 300 × 50-mm C18 column run isocratically at 1 mL/min with a mobile phase of 0.1 M ammonium acetate and 4% (vol/vol) acetonitrile. The elution of precursor UpG and products cUMP and G were monitored by UV absorbance at 260 nm (Fig. S2*A*). The fraction of reaction, $F$ = [cUMP or G]/([UpG] + [cUMP or G]), was quantified by integration of the chromatogram. The HPLC fractions containing the unreacted UpG were collected and dried under vacuum. The pellets were resuspended in 1 mL of $H_2O$, dried down three to four additional times, and finally resuspended in water at a concentration of 20–50 μM for subsequent isotopic analysis by tandem MS.

Determination of the substrate $^{16}O/^{18}O$ ratio in UpG was accomplished by tandem MS using an ABI QStar electrospray ionization quadrupole/TOF tandem mass spectrometer in negative ion mode. The sample was injected at 1–0.5 μL/min using an ion voltage of −2,200 V. The entire deprotonated molecular ion isotopic cluster of the substrate with a monoisotopic $m/z$ of 588 was isolated using low resolution in the initial quadrupole stage and fragmented by inert gas collision at a collision energy of 35 eV. In the second stage, the resulting fragments at 100–600 $m/z$ were resolved by TOF-MS. Fragmentation of the monoisotopic ion yields high-intensity product ions at $m/z$ 476 and $m/z$ 211 that result from loss of the uridine nucleobase and from ribosephosphate, respectively, as shown in Fig. S2*B*. Both species contain the enriched 2′-O, 5′-O NPO positions, and were sufficiently abundant for precise quantitation of $^{16}O/^{18}O$ ratios in the residual substrate population with 10–15 min of continuous data acquisition. The second TOF-MS dimension produces highly enhanced signal to noise as demonstrated in Fig. S2*C* for the 211/213 ion pair. The absence of background noise and the exclusion of contaminants due to the high mass resolution of the TOF result in a precision of 0.5% or better as assessed by analytical dilution of isotopic standards. Fitting the $m/z$ data to a series of Gaussian peaks was used to quantify the abundance of the two isotopologues and to determine the $^{16}O/^{18}O$ ratio (3). Alternatively, with complete baseline separation of the isotopic peaks and the absence of apparent contaminants, the Analyst (Applied Biosystems) integration routine produced equivalent results.

**Impact of Binding Commitments on Interpretation of Intrinsic KIEs for RNase A.** Because the method described above involves internal competition between two substrates in the same reaction, the observed KIE measures the ratios of the $k_{cat}/K_m$ values for the RNAs containing $^{16}O$ and $^{18}O$ (2, 4). Therefore, substrate binding steps may interfere with the KIE measurements for RNase A if dissociation is slow relative to chemistry, resulting in a "commitment" of the bound substrate to undergo the chemical transformation (5). Here, we consider in more detail the meaning of $k_{cat}/K_m$ for the UpG substrate under conditions where KIEs were measured, and the potential impact of binding commitments on the observed experimental KIE values was assessed. For the simplest mechanism in which a single form of the enzyme combines with the substrate [i.e., the middle pathway for reaction of the correctly protonated form of the enzyme (EH) and substrate (S) in Scheme **S1**, below], the

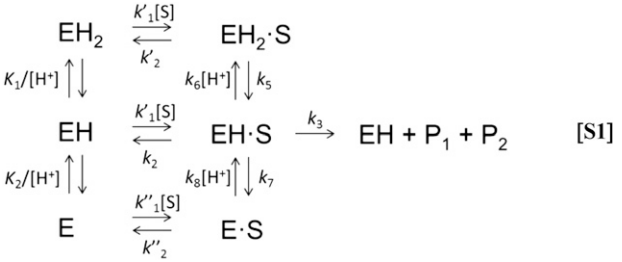

[S1]

reaction at limiting substrate concentration can be considered to follow a simple rate equation (6),

$$\frac{k_{cat}}{K_m} = \frac{k_1 k_3}{k_2 + k_3},$$

where $k_1$ and $k_2$ represent the rate constants for substrate association and dissociation, respectively, and $k_3$ is the rate constant for the conversion of bound substrate to free enzyme and product in this case. Conditions under which substrate dissociation is fast relative to the chemical step of the reaction ($k_2 > k_3$) are most favorable for measuring enzyme KIEs. Under these circumstances,

$$\frac{k_{cat}}{K_m} = \frac{k_1 k_3}{k_2 + k_3} = \frac{k_1 k_3}{k_2} = \frac{k_3}{K_d},$$

where $K_d$ is the equilibrium dissociation constant for substrate binding. Therefore, because isotope effects express the ratio of $k_{cat}/K_m$ values, they report on the difference in bonding between the substrate free in solution and in the transition state, and they can include effects on binding as well as the chemical step (7).

Alternatively, a sticky substrate, or one that can be described as having a high binding commitment, is defined as one that reacts through the first irreversible step of the reaction ($k_3$) with a rate constant that is faster than the rate constant for dissociation ($k_2$) (4, 8). The commitment factor or stickiness ratio ($C$) is defined as $k_3/k_2$ for the simple mechanism above. Under these circumstances, the observed KIE is attenuated proportionally according to Cleland and Cook (4) and Cleland (8): $^{18}k_{obs} = (^{18}k + C)/(1 + C)$.

Given this relationship, a commitment factor of *ca.* 2 would reduce an intrinsic leaving group KIE of *ca.* 1.035 to a value that is observed for RNase A (*ca.* 1.015). A proportional attenuation of the value of the observed RNase A nucleophile KIE ($^{18}k_{NUC}$; 0.994) due to a binding commitment of this magnitude would result in an intrinsic $^{18}k_{NUC}$ with an estimated magnitude of 0.988. As described in the text, the $^{18}k_{NUC}$ for this reaction is interpreted as resulting from the combined effects of O-P bond formation and deprotonation. It seems unlikely that a more inverse $^{18}k_{NUC}$ value could result from increased O-P bonding, considering that the acid-catalyzed reaction, which is fully stepwise, shows a similar inverse $^{18}k_{NUC}$ (Table 1). Also, computational models involving a transient phosphorane intermediate with advanced 2′O-P bonding are consistent with the observed KIEs (1, 9). Because the equilibrium isotope effect (EIE) for deprotonation is normal (1.015–1.024) in the direction of deprotonation, incomplete deprotonation of the 2′O would result in only partial expression of this effect in the transition state. The net effect could be a more inverse $^{18}k_{NUC}$ due to a smaller normal contribution to the observed intrinsic KIE from loss of the O-H bonding vibrational mode. However, any mechanistic scenario must necessarily account for the large (1.035) KIE on the 5′O leaving group. Taken together, these results would imply that the departure of the 5′O occurs as an oxyanion with little participation of active site functional groups offsetting the buildup of unfavorable negative charge by protonation. Thus, the estimated 2′O and 5′O KIEs, assuming attenuation of both by substrate binding commitments, do not easily correspond with expectations based on the observed solution KIEs and the proposed mechanism of RNase A from previous structural and mechanistic work.

**Analysis of the Binding Commitment for UpG Cleavage by RNase A.** Several experimental observations can be considered to gain information on the degree to which binding commitments affect the observed KIEs for RNase A. These data can include (*i*) comparison of the magnitude of observed RNase A effects relative to intrinsic KIEs on solution reactions and to values previously measured for a slow substrate, (*ii*) comparison of the reaction kinetics of UpG with those of other model substrates, (*iii*) analysis of the effects of solvent viscosity, and (*iv*) evaluation of the difference between the microscopic $pK_a$ values of active site residues measured directly and observed macroscopic $pK_a$ values from kinetic studies. The experimental data relating to these factors are discussed, in turn, below.

Importantly, the observation that the KIEs for RNase A are similar in magnitude to the values observed for solution reaction, where binding commitments are not present, argues that the chemical step is at least partially rate-limiting. This interpretation could also be consistent with the scenario described above, where the commitment factor is small and only partial expression of the intrinsic KIE is observed. Nonetheless, the leaving group KIE reported here for UpG (1.014) is similar to the value measured for uridine 3′-*m*-nitrobenzyl phosphate (1.017) reported by Cleland and colleagues (10). This slow substrate reacts with a $k_{cat}/K_m$ that is $10^4$-fold lower than uridylyl-3′-adenosine [5′-UpA-3′ (UpA)] and $10^3$ lower than UpG. Thus, the correspondence of the observed KIEs for the RNase A reaction reported here with the previously reported KIEs for solution reactions and previous effects for RNase A using a model substrate is consistent with the conclusion that the observed KIEs closely approximate the intrinsic effects.

Perspective on the rate-limiting steps for the UpG reaction can also be gained by comparing the kinetic parameters of UpG with those determined for other RNase A substrates. The $k_{cat}$ for the reaction of UpG is ~30 $s^{-1}$ (Fig. S3), which is significantly slower than UpA (1,400 $s^{-1}$) under similar reaction conditions (11). The $k_{cat}$ for uridine 3′-*p*-nitrophenol phosphate is approximately twofold slower (19 $s^{-1}$) (12). The rate constant for release of a cyclic nucleotide monophosphate is 1,500 $s^{-1}$ and has been proposed to be rate-limiting for $k_{cat}$ for fast-reacting polynucleotide substrates and for UpA (11, 13). The observed $k_{cat}$ for UpG is significantly slower and presumably represents a slow step upstream of substrate dissociation. The $k_{cat}/K_m$ for UpG is $2.7 \times 10^4$ $M^{-1}\cdot s^{-1}$, which is significantly less than the $k_{cat}/K_m$ for a UpA substrate ($2.3 \times 10^6$ $M^{-1}\cdot s^{-1}$) and similar to the value of $5.7 \times 10^4$ $M^{-1}\cdot s^{-1}$ observed for uridine-3′-*p*-nitrophenol phosphate measured under similar conditions (11, 12, 14). Therefore, the low magnitude of $k_{cat}$ for the UpG reaction relative to the $k_{cat}$ values for UpA and oligonucleotide substrates makes it unlikely that product release is rate-limiting, and the $k_{cat}/K_m$ for UpG is consistent with other slow-reacting substrates for which the chemical step is considered to be rate-limiting.

The stickiness of a substrate will also affect the observed pH profile of the reaction (4, 15), and the quantitative nature of the dependence is determined by the specific kinetic scheme (16, 17). The following kinetic scheme from Park and Raines (11) is assumed for the reaction of UpG by RNase A under $k_{cat}/K_m$ (limiting substrate concentration) conditions. Similar to other substrates, the observed pH dependence of $k_{cat}/K_m$ for the reaction of the UpG substrate (Fig. S4) is consistent with a mechanism in which there are two titratable groups important for the reaction.

The acid dissociation constants for protonation of the two functional groups assumed to be His12 and His119 are $K_1$ and $K_2$, and the second-order rate constants for association of the substrate are $k_1$, $k'_1$, and $k''_1$. The first-order rate constants for substrate dissociation are $k_2$, $k'_2$, and $k''_2$, and the chemical step is $k_3$. The rate equation for $k_{cat}/K_m$ is

$$\frac{k_{cat}}{K_m} = \frac{\left(k'_1\frac{[H^+]}{K_1} + k_1 + k''_1\frac{K_2}{[H^+]}\right)k_3}{\left(\frac{[H^+]}{K_1} + 1 + \frac{K_2}{[H^+]}\right)\left(\frac{k'_2k_6[H^+]}{k'_2 + k_5} + k_2 + k_3 + \frac{k''_2k_7}{k'_2 + k_8[H^+]}\right)}.$$

If it is assumed that proton association and dissociation are rapid relative to substrate binding rate constants, the rate equation simplifies to

$$\frac{k_{cat}}{K_m} = \frac{\left(k'_1\frac{[H^+]}{K_1} + k_1 + k''_1\frac{K_2}{[H^+]}\right)k_3}{\left(\frac{[H^+]}{K_1} + 1 + \frac{K_2}{[H^+]}\right)\left(k'_2\frac{[H^+]}{K'_1} + k_2 + k_3 + k''_2\frac{K'_2}{[H^+]}\right)},$$

where $K'_1$ and $K'_2$ are the acid dissociation constants in the presence of the bound substrate. The issue of whether the protons bound to the RNase A active site are themselves sticky in the presence of the bound substrate is not known. However, given the slow reactivity of the UpG substrate and the fact that the dynamic motions of the enzyme occur with much faster rate constants, this assumption appears reasonable. If the substrate is not sticky and $k_2$ is large, the rate equation reverts to its simple form, which is used to fit the pH profile data in Fig. S4. The observed kinetic $pK_a$ values are assumed to approximate the intrinsic enzyme acid dissociation constants $K_1$ and $K_2$ in Scheme **S1**.

As described previously (4, 11, 15), for a sticky substrate, the presence of binding commitments can result in alteration of the pH profile of the reaction such that the observed macroscopic $pK_a$s do not correspond to the intrinsic microscopic $pK_a$s of the titratable groups involved in the reaction. The observed macroscopic $pK_a$ for the reaction of UpG is 5.2, whereas the predicted $pK_a$ under similar reaction conditions is 5.6, as described previously by Park and Raines (11). If the observed macroscopic $pK_a$ represents His12, the difference between these values is an estimation of the binding commitment according to the following: $pK_{app} = pK_1 - \log(1 + C)$.

Thus, the difference of 0.4 between the observed and predicted $pK_a$ values could potentially reflect a small binding commitment of ~1.5. A substrate binding commitment of this magnitude would be sufficient to reduce an intrinsic KIE of 1.035 to the value of 1.014 observed for RNase A as discussed above. On the other hand, the observed $pK_a$ for the acidic functional group, assumed to be His119, is 6.3, which is less than the predicted value of 6.6. The presence of a significant binding commitment would result in an apparent increase in the $pK_a$ in this instance, and this expectation does not hold. Thus, these data indicate that under conditions in which KIE measurements were performed at pH 7, which is above the $pK_a$ of the general acid, the substrate binding commitments are minimal.

However, as pointed out previously (11), there are two scenarios in which the substrate can be sticky and there will still be minimal effect on the observed $pK_a$ relative to its intrinsic value. The first occurs if release of the proton from EH·S ($k_7$) is slow relative to substrate dissociation ($k_2$); however, as indicated above, this is unlikely to be the case for the UpG substrate. The second occurs when the rate constant for association with EH is much faster than with the form of the enzyme in which neither active site functional groups are protonated (E) ($k_1 > k''_1$). Although the magnitudes of the rate constants for association of substrates with the different protonated forms of the enzyme are not known, the binding of the anionic substrate to the mono- or deprotonated active site is likely to occur with a greater rate constant than to the fully deprotonated form. Indeed, the higher affinity of an oligodeoxynucleotide substrate mimic at low pH has been demonstrated previously (18). Thus, although these data do not provide direct evidence for the relative magnitudes of $k_3$ and $k_2$, the observed pH dependence of the reaction is consistent with mechanisms in which there are minimal binding commitments.

The effect of viscosity on $k_{cat}/K_m$ values can also provide information on substrate stickiness. In the mechanism shown above, the chemical step $k_3$ is independent of solvent viscosity (because it is intramolecular within the active site), and steps associated with substrate binding and product dissociation are assumed to be inversely proportional to the solvent viscosity. Accordingly, if viscosity does not affect $k_{cat}/K_m$, this result is consistent with low binding commitments because it is assumed that viscosity equally affects $k_1$ and $k_2$. If product release limits $k_{cat}/K_m$, the observed rate will decrease even if the substrate is not sticky. As shown in Fig. S5, the $k_{cat}/K_m$ of the UpG substrate is essentially insensitive to concentrations of glycerol, which increase the solution viscosity sufficiently to perturb macromolecular association and dissociation processes. Therefore, the insensitivity of the observed $k_{cat}/K_m$ to viscosity under the conditions in which KIEs were measured is consistent with a mechanism in which there are low binding commitments and the product release step is not rate-limiting. As indicated above, the $k_{cat}$ for UpG is significantly slower than the protein dynamics that are proposed to be rate-limiting for fast substrates. As demonstrated by Thompson (12), the $k_{cat}/K_m$ for the faster UpA substrate decreases with increasing solvent viscosity in a manner consistent with rate-limiting substrate association, whereas the reaction of uridine-3′-*p*-nitrophenol phosphate was not sensitive. Therefore, the observed insensitivity of the UpG reaction to increasing glycerol is consistent with a mechanism in which a step other than association or product release is rate-limiting.

**Computational Evaluation of Alternative Transition State Models.** To define the structure of the RNase A transition state better and evaluate the potential for active site interactions to influence charge distribution and the resulting KIEs, we analyzed a total of five models: two nonenzymatic models and three enzymatic models. The transition states of these five models are depicted in Fig. S6, whereas their calculated KIE values are listed in Table S1. The results with these five model systems were used to guide the quantum mechanical calculations presented in the main text, which involve a more complex structure, including the adjacent ribose structure, as shown in Fig. S4.

The first nonenzymatic model (denoted as 1stNonEnzyme in Fig. S6) is an ethylene glycol phosphate methyl ester reacting under alkaline conditions. In this model, we assume that the deprotonation occurs in a preequilibrium that is not rate-limiting. As seen in Table S1, the calculated KIEs for this model are consistent with experimental results for the base-catalyzed 2′-*O*-transphosphorylation of the RNA dinucleotide 5′-UpG-3′ (2). More details and discussions, as well as further insights provided by this model and other relevant models, can be found in the paper by Wong et al. (1).

In the second nonenzymatic model (denoted as 2ndNonEnyzme in Fig. S6), we examined the effect of adding a proton at O2′ in the reactant state. This model was constructed to evaluate the potential for a proton transfer first from O2′ to O1P and then from the O1P position to the 5′O leaving group in the rate-limiting transition state of the solution reaction catalyzed by specific acid. In comparison to the first nonenzymatic model, the KIE value of the leaving group ($^{18}k_{LG}$) drops from 1.059 to 1.046 due to the concomitant proton transfer. This suggested that the decreased magnitude of $^{18}k_{LG}$ relative to the specific base reaction could also be due to concomitant proton transfer (i.e., general acid catalysis). However, the lack of a large thio effect on the RNase A reaction and the relatively smaller normal value of $^{18}k_{LG}$ we observe both argue against complete proton transfer from an NPO position to the 5′O leaving group in the RNase A reaction.

Consequently, based on our second nonenzymatic model mentioned above, which has a proton at O2′ in the reactant state, we built our first enzymatic model (denoted as 1stEynzme in Fig. S6) by testing the effect of adding a single protonated imidazole. This protonated imidazole is hydrogen-bonded with O5′ in the reactant state and transfers a proton to O5′ in the transition state. This model was constructed to probe the possibility of a proton transfer from O2′ to an NPO, followed by proton transfer from the protonated imidazole (instead of from the NPO) to the 5′O leaving group. In other words, the protonated imidazole is the general acid and the proton at O1P does not move in the rate-limiting transition state of our first enzymatic model (Fig. S6). As seen in Table S1, in contrast to our second nonenzymatic model, the value of $^{18}k_{LG}$ significantly drops from 1.046 to 1.010. This indicates substantial offset of the magnitude of this KIE by concomitant proton transfer in the transition state of which the protonated imidazole acts as the general acid and O1P stays protonated. However, the calculated KIE value of the NPO effect ($^{18}k_{NPO}$) is small and inverse this time (Table S1), which is inconsistent with the experimentally observed small normal values. Again, the lack of a large thio effect on the RNase A reaction and the small normal value of $^{18}k_{NPO}$ we observe both argue against protonation at an NPO position in the rate-limiting transition state in the RNase A reaction.

Therefore, we built the second and the third enzymatic models (denoted as 2ndEynzme and 3rdEnzyme, respectively, in Fig. S6) to test the effect of removing the proton at the O1P position in the transition state. In addition, in our third enzymatic model, we positioned a second protonated imidazole ring that is hydrogen-bonded with O1P in the transition state (Fig. S6). Initially, we had a hard time locating a late transition state for the 2ndEynzme model because the potential energy surface is quite flat. In contrast, the transition state was readily identified for our third enzymatic model. Moreover, this model most closely approximates the observed RNase A KIEs (Table S1), which show a normal value for $^{18}k_{LG}$, near-inverse unity for $^{18}k_{NUC}$, and near-normal unity for $^{18}k_{NPO}$. Therefore, the enzymatic model presented in Fig. 4 was built with two protonated imidazoles based on the results from the 3rdEynzme model. One imidazole is hydrogen-bonded with O1P, and another functions as the gen-

eral acid for the 5′O leaving group in the transition state. The model in Fig. 4 also includes a more realistic ribose-like sugar ring and ethoxide leaving group. This model supports a scenario that His12 (or other candidates) accepts a proton from O2′, Lys41 (or His12 or other candidates) H-bonded with NPO and that His119 donates the proton to the leaving O5′.

Moreover, our approach for modeling the transitions states for solution and RNase A-catalyzed RNA 2′-*O*-transphosphorylation reactions differs from previous methods used to model the transition states by Schramm and colleagues (19). The transition states modeled in the present study are fully optimized without any constraint, including without the constraint of matching the experimental KIE values. By definition, a transition state should be at a stationary point of the reactive potential energy surface, that is, at a point where the force or gradient of the potential energy surface is zero. Additionally, it should have only a single imaginary frequency. Both of these criteria are met by the transition states reported in this work. From our previous work, we showed that the hybrid B3LYP exchange correlation density functional is accurate enough for successfully characterizing the reaction paths and transition states, as well as the effects of thio substitutions on the nonbridging oxygens (1).


1. Wong KY, et al. (2012) Characterization of the reaction path and transition states for RNA transphosphorylation models from theory and experiment. *Angew Chem Int Ed Engl* 51(3):647–651.
2. Harris ME, et al. (2010) Kinetic isotope effects for RNA cleavage by 2′-O-transphosphorylation: Nucleophilic activation by specific base. *J Am Chem Soc* 132(33):11613–11621.
3. Cassano AG, et al. (2007) Inaccuracies in selected ion monitoring determination of isotope ratios obviated by profile acquisition: Nucleotide 18O/16O measurements. *Anal Biochem* 367(1):28–39.
4. Cleland WW, Cook PF (2007) *Enzyme Kinetics and Mechanism* (Garland, New York).
5. Cleland WW (2005) The use of isotope effects to determine enzyme mechanisms. *Arch Biochem Biophys* 433(1):2–12.
6. Cleland WW (1975) Partition analysis and the concept of net rate constants as tools in enzyme kinetics. *Biochemistry* 14(14):3220–3224.
7. Schramm VL (2007) Binding isotope effects: Boon and bane. *Curr Opin Chem Biol* 11(5):529–536.
8. Cleland WW (1982) Use of isotope effects to elucidate enzyme mechanisms. *CRC Crit Rev Biochem* 13(4):385–428.
9. Radak BK, Harris ME, York DM (2013) Molecular simulations of RNA 2′-O-transesterification reaction models in solution. *J Phys Chem B* 117(1):94–103.
10. Sowa GA, Hengge AC, Cleland WW (1997) 18O isotope effects support a concerted mechanism for ribonuclease A. *J Am Chem Soc* 119(9):2319–2320.
11. Park C, Raines RT (2003) Catalysis by ribonuclease A is limited by the rate of substrate association. *Biochemistry* 42(12):3509–3518.
12. Thompson JE, et al. (1995) Limits to Catalysis by Ribonuclease A. *Bioorg Chem* 23(4): 471–481.
13. Watt ED, Shimada H, Kovrigin EL, Loria JP (2007) The mechanism of rate-limiting motions in enzyme function. *Proc Natl Acad Sci USA* 104(29):11981–11986.
14. Thompson JE, Raines RT (1994) Value of general Acid-base catalysis to ribonuclease a. *J Am Chem Soc* 116(12):5467–5468.
15. Cleland WW (1977) Determining the chemical mechanisms of enzyme-catalyzed reactions by kinetic studies. *Adv Enzymol Relat Areas Mol Biol* 45:273–387.
16. Cook PF, Cleland WW (1981) pH variation of isotope effects in enzyme-catalyzed reactions. 1. Isotope- and pH-dependent steps the same. *Biochemistry* 20(7):1797–1805.
17. Cook PF, Cleland WW (1981) pH variation of isotope effects in enzyme-catalyzed reactions. 2. Isotope-dependent step not pH dependent. Kinetic mechanism of alcohol dehydrogenase. *Biochemistry* 20(7):1805–1816.
18. Park C, Schultz LW, Raines RT (2001) Contribution of the active site histidine residues of ribonuclease A to nucleic acid binding. *Biochemistry* 40(16):4949–4956.
19. Schramm VL (2011) Enzymatic transition states, transition-state analogs, dynamics, thermodynamics, and lifetimes. *Annu Rev Biochem* 80:703–732.

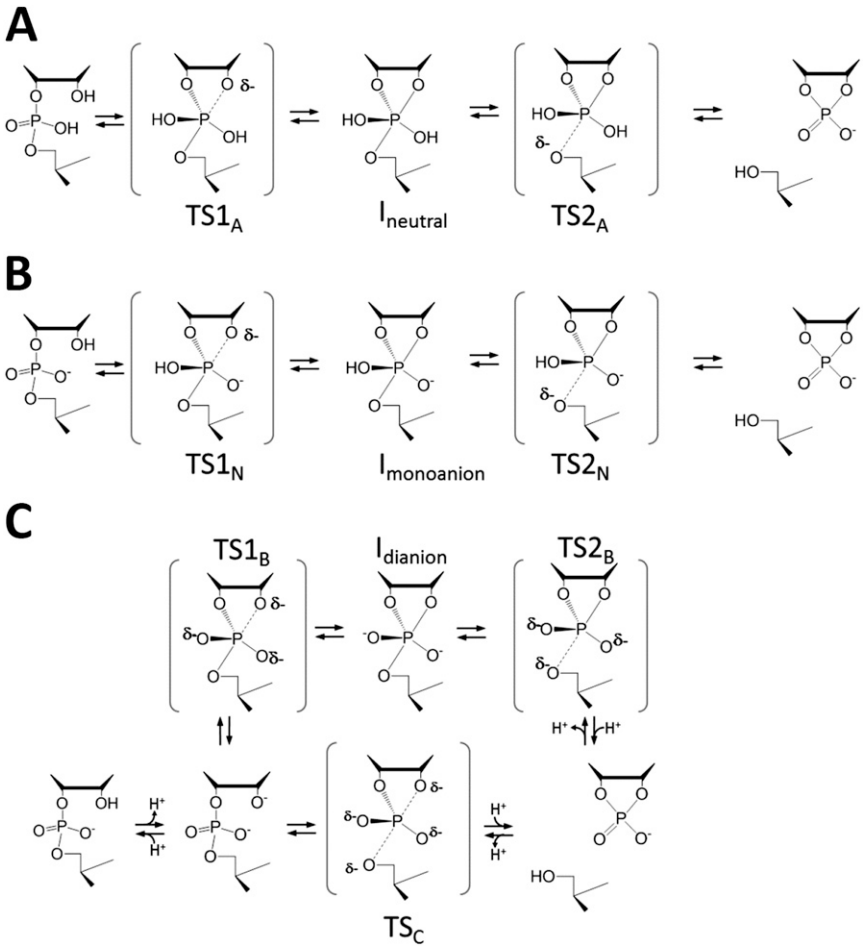


**Fig. S1.** Potential reaction schemes for RNA 2′-*O*-transphosphorylation. (*A*) Stepwise mechanism for acid catalysis involves the formation of a neutral phosphorane intermediate ($I_{neutral}$). (*B*) Stepwise mechanism for acid catalysis with formation of a monoanionic phosphorane intermediate ($I_{monoanion}$). (*C*) Concerted and stepwise mechanism with formation of an anionic phosphorane intermediate ($I_{dianion}$) for base catalysis. TS, transition state.

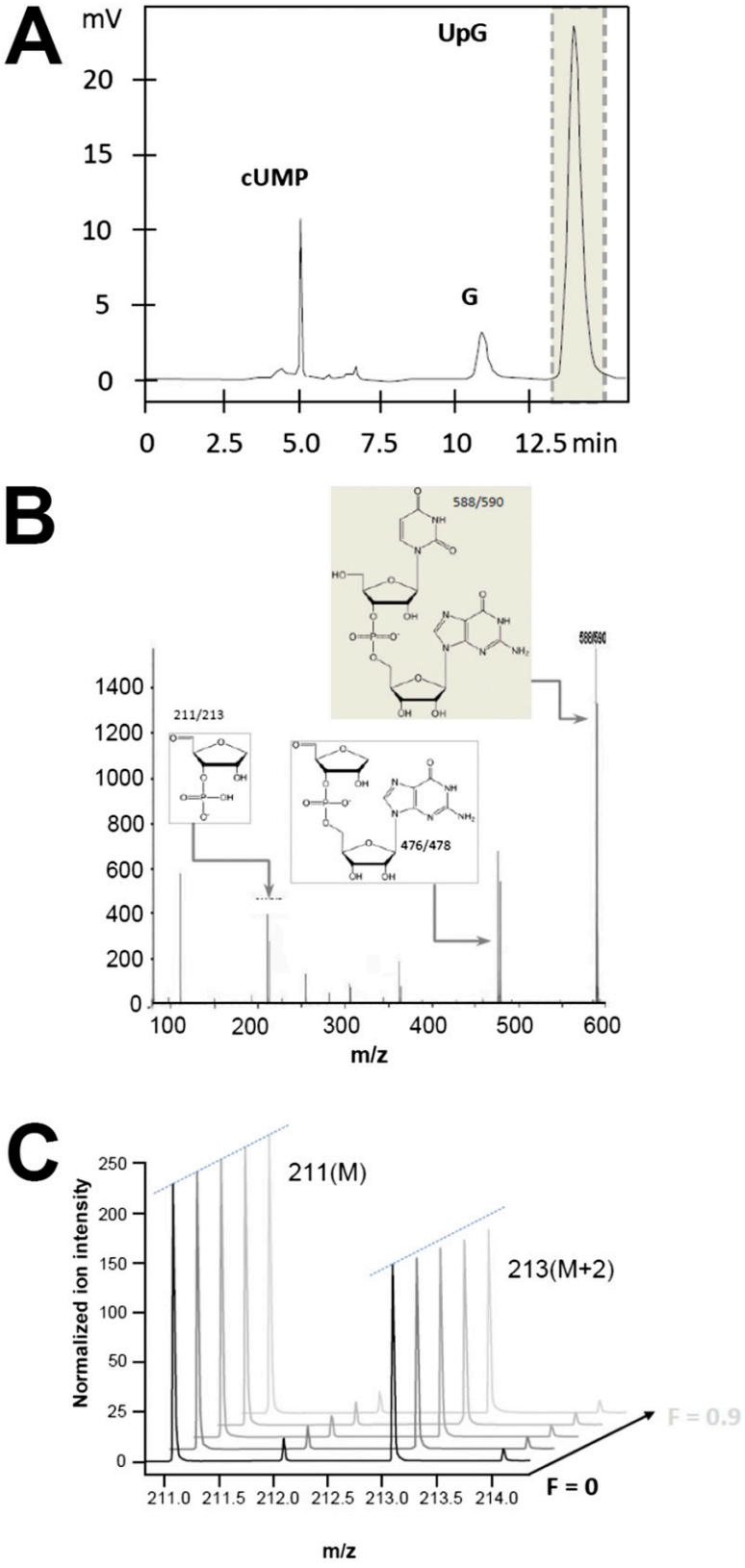


**Fig. S2.** Determination of KIEs on RNA 2′-*O*-transphosphorylation reactions by internal competition. (*A*) RP-HPLC separation of substrate UpG and products cUMP and G. (*B*) TOF product ion spectrum of UpG showing the *m/z* 211/213 and 476/478 ions used to compute $^{18}O/^{16}O$ isotope ratios. The structures of the molecular ion *m/z* 588/590 and product ions used to compute the KIEs are shown. (*C*) Close-up of mass spectrum of the *m/z* 211/213 product ions showing the high level of signal to noise, consistent peak shape, and mass resolution obtainable. A cartoon of overlain spectra is shown, indicating results from samples for the same reaction that are analyzed at early (black, dark gray) and progressively higher fractions of reaction (progressively lighter gray). The change in the relative areas of the 211 (M) and 213 (M + 2) peaks is used to compute the isotope effect. The relative heights of the two peaks are indicated by dashed lines.

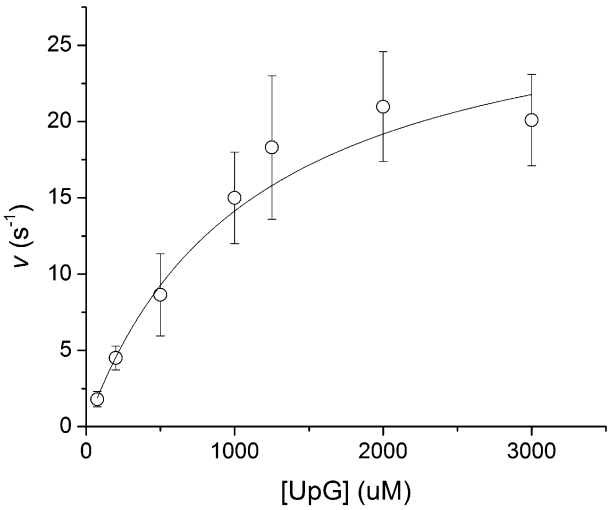


**Fig. S3.** Multiple turnover kinetics of UpG cleavage by RNase A. The steady-state reaction rates ($v_{obs}/E_{total}$) were determined at substrate concentrations ranging from 75 to 3,000 μM UpG in 0.1 M NaCl, 10 mM bis-Tris (pH 7.0), and 40 nM enzyme. The conversion of substrate UpG to product cUMP and G was quantified by analysis of reaction time points by RP-HPLC as shown in Fig. S2*A,* followed by integration of the chromatograms to determine the fraction of reacted substrate. Initial rates were determined from the slope of linear fits of the fraction of the reacted substrate vs. time at less than 10% conversion of the total substrate concentration. These data were fit to the Michaelis–Menton equation [$v = k_{cat}/(1 + K_m/[UpG])$] to estimate $k_{cat}$ ($30 \pm 3\ s^{-1}$), $K_m$ (1,100 ± 200 μM), and $k_{cat}/K_m$ [2.7 (±0.8) × $10^4$ $M^{-1}{\cdot}s^{-1}$).

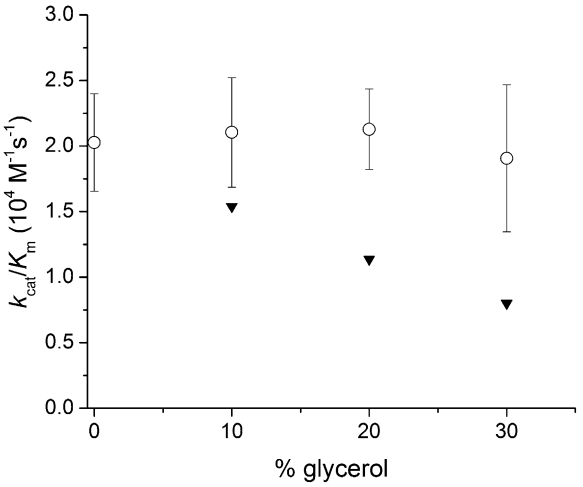


**Fig. S4.** Dependence of $k_{cat}/K_m$ on glycerol concentration. The steady-state reaction rates ($v_{obs}/E_{total}$) were determined as described in the legend for Fig. S3, with the exception that conversion of UpG to product was quantified using UV absorbance spectroscopy. Solutions of enzyme and substrate at 2× concentration were mixed by stopped flow using an Applied Photophysics pi*-180 spectrometer, and the change in absorbance at 260 nm was monitored. Due to the decreased absorbance in the UpG substrate relative to the free nucleoside and nucleotide products, the absorbance increases on product formation. The Δε was determined by taking spectra (220–350 nm) of samples before and after the reaction, with the complete conversion to product confirmed by RP-HPLC. The observed $k_{cat}/K_m$ values in the absence of glycerol and in the presence of increasing glycerol concentrations are shown.

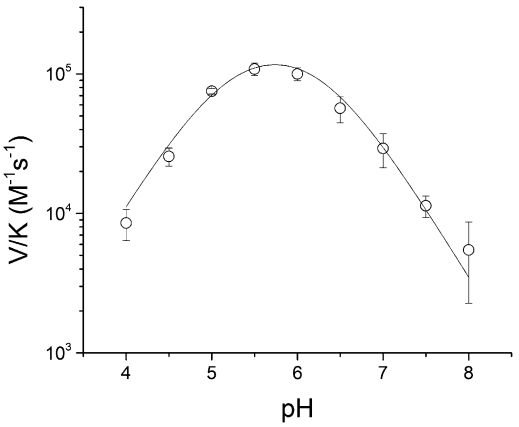


**Fig. S5.** Dependence of $k_{cat}/K_m$ on pH. The observed $k_{cat}/K_m$ values for steady-state reactions of UpG were determined at pH values from 4 to 8 as described in the legend for Fig. S3, with the exception that buffers at different pH values were used. Conversion of UpG to product was quantified by UV spectroscopy as described in Fig. S4. The following buffers were used: pH 4–4.5, acetate; pH 5–6.5, MES; and pH 7–8, Tris. To estimate the macroscopic $pK_a$ values, the data were fit to $k_{cat}/K_m = (k_{cat}/K_m)_{max}/(1 + 10^{(pH-pK1)} + 10^{(pK2-pH)})$, where the values of pK1 and pK2 are interpreted according to the mechanism discussed in *SI Text* and correspond to the acid dissociation constants $K_1$ and $K_2$ in Scheme **S1**.

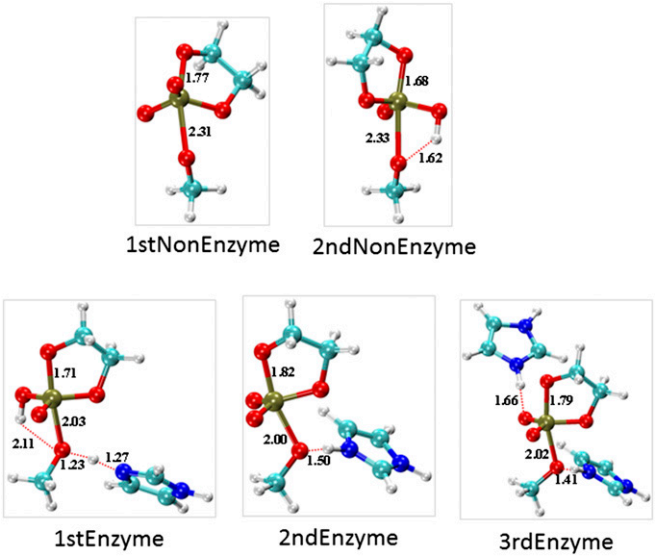


**Fig. S6.** Alternative solution and enzymatic models. (*Upper*) Two nonenzyme models, 1stNonEnzyme and 2ndNonEnzyme, are shown. (*Lower*) Three enzyme models, 1stEnzyme, 2ndEnzyme, and 3rdEnzyme, are shown. The rationales for construction of these models and the resulting computed KIE values are described in *SI Text*. Key bond lengths are indicated in angstroms.

**Table S1. Comparison of calculated KIEs for enzymatic and nonenzymatic models of RNA 2′-O-transphosphorylation**

| Model system | $^{18}k_{LG}$ | $^{18}k_{NUC}$ | $^{18}k_{NPO}$ |
|---|---|---|---|
| QM nonenzymatic model | | | |
| 1stNonEnzyme | 1.059 | 0.968 | 1.004 |
| 2ndNonEnzyme | 1.046 | 0.990 | 1.000 |
| QM enzymatic model | | | |
| 1stEnzyme | 1.010 | 0.988 | 0.995 |
| 2ndEnzyme | 1.038 | 0.997 | 1.006 |
| 3rdEnzyme | 1.037 | 0.995 | 1.004 |
| RNase A | 1.014 | 1.014 | 1.001 |

QM, quantum mechanics.